Clinical Biomechanics 64 (2019) 2–13

Contents lists available at ScienceDirect

Clinical Biomechanics

journal homepage: www.elsevier.com/locate/clinbiomech

Mechanoporation is a potential indicator of tissue strain and subsequent degeneration following experimental traumatic brain injury☆

Michelle C. LaPlaca[a,*], M. Christian Lessing[a], Gustavo R. Prado[a], Runzhou Zhou[b], Ciara C. Tate[a], Donna Geddes-Klein[c], David F. Meaney[c], Liying Zhang[b]

[a] Wallace H. Coulter Department of Biomedical Engineering, Georgia Institute of Technology and Emory University, 313 Ferst Dr., Atlanta, GA 030332-0535, USA
[b] Department of Biomedical Engineering, Wayne State University, 818 W Hancock St., Detroit, MI 48201, USA
[c] Department of Bioengineering, University of Pennsylvania, 210 South 33rd St., Philadelphia, PA 19104-6321, USA

ARTICLE INFO

Keywords:
Traumatic brain injury
Membrane permeability
Mechanoporation
Hippocampus
Finite element model
Neuronal degeneration

ABSTRACT

Background: An increases in plasma membrane permeability is part of the acute pathology of traumatic brain injury and may be a function of excessive membrane force. This membrane damage, or mechanoporation, allows non-specific flux of ions and other molecules across the plasma membrane, and may ultimately lead to cell death. The relationships among tissue stress and strain, membrane permeability, and subsequent cell degeneration, however, are not fully understood.

Methods: Fluorescent molecules of different sizes were introduced to the cerebrospinal fluid space prior to injury and animals were sacrificed at either 10 min or 24 h after injury. We compared the spatial distribution of plasma membrane damage following controlled cortical impact in the rat to the stress and strain tissue patterns in a 3-D finite element simulation of the injury parameters.

Findings: Permeable cells were located primarily in the ipsilateral cortex and hippocampus of injured rats at 10 min post-injury; however by 24 h there was also a significant increase in the number of permeable cells. Analysis of colocalization of permeability marker uptake and Fluorojade staining revealed a subset of permeable cells with signs of degeneration at 24 h, but plasma membrane damage was evident in the vast majority of degenerating cells. The regional and subregional distribution patterns of the maximum principal strain and shear stress estimated by the finite element model were comparable to the cell membrane damage profiles following a compressive impact.

Interpretation: These results indicate that acute membrane permeability is prominent following traumatic brain injury in areas that experience high shear or tensile stress and strain due to differential mechanical properties of the cell and tissue organization, and that this mechanoporation may play a role in the initiation of secondary injury, contributing to cell death.

1. Introduction

Traumatic brain injury (TBI) is produced by suprathreshold mechanical loading of the head that transduces stress and strain to the brain, causing primary damage and triggering secondary injury events. The plasma membrane is the first line of defense for a cell, and physical breach under mechanical loading can lead to non-specific flux of ions and molecules into and out of the cell. Traumatically-induced plasma membrane damage—mechanoporation—in both axons and somata, has been observed across many experimental models of traumatic central nervous system (CNS) injury and is considered a part of the acute injury response (Pettus et al., 1994, Povlishock and Pettus, 1996, LaPlaca et al., 1997, Geddes et al., 2003a, 2003b, Singleton and Povlishock, 2004, Stone et al., 2004, Farkas et al., 2006, Cho et al., 2007, Kilinc et al., 2008, Whalen et al., 2008, Simon et al., 2009, LaPlaca and Prado, 2010, Cullen et al., 2011). Plasmalemma compromise is associated with calcium influx and general ion dysregulation, as well as rapid onset of faulty signaling and degradative cellular processes (Geddes et al., 2003a, 2003b; Kilinc et al., 2009; LaPlaca et al., 1997; Okonkwo et al., 1998; Pettus and Povlishock, 1996; Singleton and Povlishock, 2004; Whalen et al., 2008). Whether membrane permeability sets the course for cell death, however, likely depends on the level of membrane

☆ Conflicts of interest: none.

* Corresponding author at: Wallace H. Coulter Department of Biomedical Engineering at Georgia Tech and Emory, Georgia Institute of Technology, 313 Ferst Dr., Atlanta, GA 30332-0535, USA.
E-mail address: michelle.laplaca@bme.gatech.edu (M.C. LaPlaca).

https://doi.org/10.1016/j.clinbiomech.2018.05.016
Received 28 October 2017; Received in revised form 25 May 2018; Accepted 31 May 2018

damage, resealing capacity of the cell, and course of secondary injury (Farkas et al., 2006; Mbye et al., 2012; Whalen et al., 2008).

While direct measurement of cell and tissue level strain during mechanical loading is technically challenging, computer simulations of TBI are quite useful in creating a spatial map of stress and strain at the millisecond time scale (Dixit and Liu, 2016; Kleiven, 2006; Mao et al., 2006; Yang and King, 2003). The brain has a complex organization and cell density and organization, in addition to tissue composition, can affect the mechanical response to a high rate traumatic load. Mechanical susceptibility, coupled with deleterious acute responses, such as inflammation and free radical production, can damage membranes and contribute to damage beyond the mechanical trigger. The hippocampus is a subcortical area that has been consistently shown to be vulnerable to secondary injury and cell death during acute post-injury periods following experimental TBI (Lowenstein et al., 1992, Hicks et al., 1993, Smith et al., 1994, Raghupathi and McIntosh, 1996, Carbonell and Grady, 1999, Grady et al., 2003, Gao et al., 2011). With similar subregional distribution, membrane compromise has been shown in the hippocampus (Singleton and Povlishock, 2004; Whalen et al., 2008), suggesting that primary mechanical damage, at least in part, may contribute to or trigger secondary injury. To this end, we aimed to investigate a possible link stress and strain patterns, cell permeability alterations, and subsequent cell death following controlled cortical impact (CCI) injury in the rat. We hypothesized that the hippocampus undergoes increasing stress and strain that mechanoporation may be an indicator of mechanical response and subsequent cellular damage.

2. Materials and methods

2.1. Animal preparation with permeability marker

All animal procedures were approved by the Institutional Animal Care and Use Committee at the Georgia Institute of Technology and the University of Pennsylvania. An exclusion dye assay and CCI were performed as previously described (Laplaca and Lessing, 2012). The initial surgical procedure consisted of permeability marker (3000 Da dextran-tetramethylrhodamine (TRITC-dextran) or Lucifer yellow, 457 Da; Molecular Probes, Eugene, OR) injection into the cerebrospinal fluid (CSF) via intrathecal injection 2 h prior to injury to allow the dye to diffuse throughout the brain. Two different sized markers were chosen to investigate a range of potential pores that have been found in similar models (Singleton and Povlishock, 2004; Whalen et al., 2008). Specifically, Sprague-Dawley male rats (average 275 g; Charles River, Wilmington, MA) were anesthetized (5% isoflurane; maintenance, 2–4% isoflurane). Rats were immobilized in a stereotactic apparatus, and a 0.5 cm transverse incision was made at the base of the skull, exposing the atlanto-occipital membrane. The membrane was punctured and polyethylene-10 tubing was gently and slowly inserted caudally into the subdural space. A 50 μl Hamilton syringe (Reno, NV) with a 30-gauge needle was connected with the tubing and used to inject the permeability marker (20 μl of 25 mg/ml (TRITC-dextran) or 4% *w/v* (Lucifer yellow) in sterile physiological saline) at a rate of 2 μl/min. The total rat cerebrospinal fluid (CSF) volume is ~250 μl and its production rate of 2 μl/min is matched with outflow (Davson et al., 1970). It is recommended to maintain CSF infusion rate < 10 μl/min and infusion volume < 10% of the total volume (Rieselbach et al., 1962). Five minutes were allowed to elapse before the tubing was slowly removed. Following the injection, the surgery site was closed and the rats were returned to their cages for 5 h to allow the permeability marker to diffuse throughout the brain.

2.2. Controlled cortical impact (CCI) injury

Two hours following injection, animals were re-anesthetized with isoflurane (5% induction, 2–4% maintenance) and secured in a stereotactic apparatus where a midline incision was made to expose the skull. A 6.0 mm diameter craniectomy was performed over the left fronto-parietal cortex, with the center 3.0 mm posterior to bregma and 3.0 mm lateral to the midline. Injured animals received a controlled cortical impact (3 m/s velocity, 2 mm depth, 250 ms dwell time, 15° from vertical) from a pneumatic piston with a 6 mm diameter impactor tip (Pittsburgh Precision Instruments, Pittsburgh, PA). Sham animals received all surgical procedures including craniectomy but were not injured. Following surgery or injury the scalp was closed. Naïve animals received the initial procedure of dye injection, but no craniectomy injury. A total of 37 rats were used for the study. The acute group (10 min post-CCI sacrifice) included: injury with TRITC-dextran ($n = 6$); injury with Lucifer yellow ($n = 5$); sham operated with TRITC-dextran ($n = 6$); sham operated with Lucifer yellow ($n = 4$); and naïve with Lucifer yellow ($n = 4$). Two groups were allowed to survive to 24 h to examine prolonged membrane permeability and cell degeneration: CCI injury with TRITC-dextran ($n = 6$) and sham operated with TRITC-dextran ($n = 6$).

2.3. Tissue processing

At the prescribed survival time, animals received an overdose of sodium pentobarbital (80 mg/kg; intraperitoneal injection) and were perfused transcardially with phosphate buffered saline (PBS) followed by 4% paraformaldehyde and 0.1% glutaraldehyde in PBS at 4 °C. The brains were harvested, immersed overnight in 4% paraformaldehyde at 4 °C, then cryoprotected with 30% sucrose. The brains were then embedded in optimal temperature cryoembedding medium (Tissue-Tek, Torrence, CA), frozen, and stored at −80 °C. Brains were serially sectioned on a cryostat (Leica CM3050S, Wetzlar, Germany) into 20 μm thick coronal sections.

Degenerating neurons were identified with Fluoro-Jade B staining (Millipore, Billerica, MA) as described previously (Schmued and Hopkins, 2000). Slides were first thawed and rinsed to remove cryoembedding compound and then heated to 50 °C for 30 min. Slides were then soaked in 100% ethanol for 3 min, 70% ethanol for 1 min, and deionized water for 1 min. Fluoro-Jade staining solution (0.0001% Fluoro-Jade B in 0.1% acetic acid with 0.00001% DAPI to visualize cell nuclei) was made immediately before staining, and slides were submerged in the solution for 1 h in the dark at 4 °C. Slides were then rinsed 3 times in deionized water, dried, rinsed in xylene, and coverslipped. A background quenching step was eliminated from the procedure to minimize the reduction of TRITC-dextran permeability marker fluorescence. Lucifer yellow sections were counterstained with TRITC-conjugated FluoroNissl (Molecular Probes, Eugene, OR). In order to identify the phenotype of permeable cells neurons and astrocytes were identified with immunohistochemistry in a subset of sections using monoclonal antibodies against neuronal nuclei (NeuN; 1:500 dilution; Millipore, Billerica, MA) and glial fibrillary acidic protein (GFAP; 1:500 dilution, Millipore) respectively.

2.4. Quantification of permeable and degenerating cells

Three coronal sections taken 100 μm apart through the corresponding injury region (for injured, sham, and naïve brains) were imaged on a Nikon Eclipse 80*i* microscope (Nikon Instruments Inc., Melville, NY) with appropriate fluorescent filters. Regions of interest included Cornu Ammonis (CA1–4) and dentate gyrus subregions of the hippocampal formation), superficial cortex, deep cortex, and striatum, for the ipsilateral and contralateral sides. Boundaries were mapped using Neurolucida software (MBF Bioscience, Williston, VT) and cells positive for TRITC-dextran, Lucifer yellow, or Fluoro-Jade in those subregions were counted and averaged over sections. Cell counts were normalized to the area of the subregion in which they were counted. In the case of double stained TRITC-dextran and Fluoro-Jade sections, the total number of stained cells was used to calculate the percentage of permeable and degenerating cells. To visualize the density of permeable

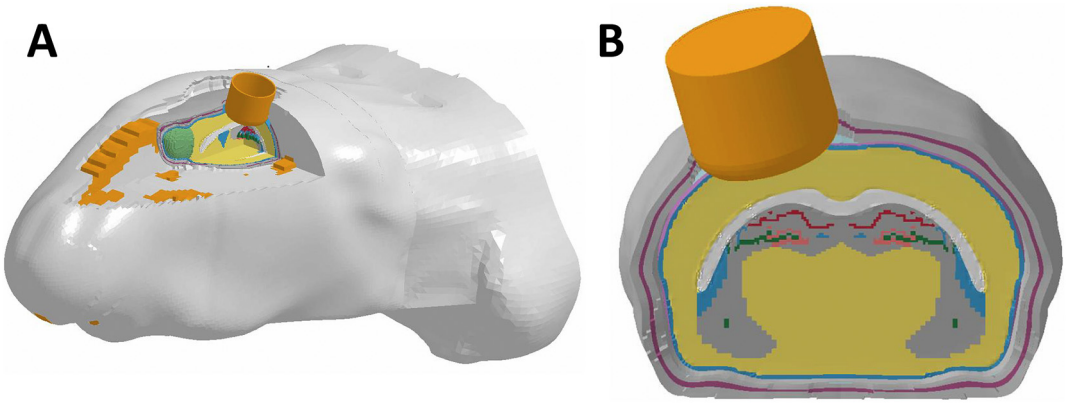

Fig. 1. Finite element model. The detailed high resolution finite element rat head model (A) with explicit presentation of the hippocampal subregions, seen in the magnified coronal section (B). There are over 2,400,000 hexahedral elements in the 3-D model.

cells in the hippocampus, MATLAB (The MathWorks, Natick, MA) was used to transform and plot the Cartesian XY coordinates of the locations of permeable cells.

A representative injured brain was quantified using design-based stereology as a quality control measure (Bukhatwa et al., 2009; Inman et al., 2005). The percentage of Lucifer yellow positive cells to total number of Nissl positive cells in ipsilateral and contralateral CA1/CA2, CA3, dentate gyrus, superficial cortex, deep cortex, and striatum was estimated using the optical fractionator method (Stereo Investigator software; Microbrightfield, Williston, VT). The percentage of Lucifer yellow positive cells for each brain region was then averaged over four 20 μm sections at 100 μm intervals for an anterior (−1.6 mm AP), center (−3.0 mm AP), and posterior (−4.4 mm AP) location within the injury (12 sections total, coefficient of error ≤ 0.1).

2.5. Statistics

Two-way repeated measures ANOVAs were performed with injury group and subregion as factors followed by Tukey test pairwise comparisons (SigmaStat Software, Systat, San Jose, CA). For stereology analysis, a general linear model ANOVA, followed by Tukey's pairwise comparisons was used to compare the percentage of Lucifer yellow positive cells 1) between ipsilateral versus contralateral sides, 2) across different brain regions on the ipsilateral side, and 3) across the relative position within the cavity. An alpha value of 0.05 was used to assess if the means were significantly different. Data are reported as mean (standard error of the mean), unless indicated otherwise.

2.6. Comparison of strain levels to membrane permeability

In order to assess membrane permeability in direct response to prescribed strain level, we injured an organotypic hippocampal sections using an in vitro equbiaxial stretch system (Geddes et al., 2003a, 2003b). Hippocampi were dissected from six-day old rat pups and sliced into 350 μm sections. Tissue was plated on silicone substrates that were precoated with laminin (50 μg/ml) and poly-L-lysine (200 μg/ml) and rocked to facilitate gas exchange at 37 °C, 5% CO_2 for 7 to 10 days in Neurobasal-A media supplemented with B-27 and glutamine / 0.65% glucose (Egert et al., 1998, De Simoni and My Yu, 2006). On the day of injury, cultures were incubated in Alexa Fluor 488 hydrazide (0.1 mM; MW = 570.48) for 10 min, then mounted into a custom injury chamber. A biaxial strain was imposed by applying a rapid pressure pulse (15 ms onset, 50 ms duration). The magnitude of the strain field was controlled by varying the chamber pressure; pressures of 4.6 and 6.75 psi corresponded to 0.5 and 0.75 strains, respectively. Following a single stretch injury at either 0 (n = 5), 50% (n = 6), or 75% (n = 6), cultures were rinsed and fixed with 4% paraformaldehyde. Fixed tissue was cut into 20 μm sections and nuclei counterstained with Hoechst 33,342 (20 μg/ml). Cells were counted in the CA1, CA3, CA4, and dentate gyrus subregions of the hippocampus and normalized to total pyramidal layer of the corresponding subregion (see Fig. 6A). Data are presented as means (standard error of the mean). Significance was assessed using Student's t-tests ($P < 0.05$ considered significant).

2.7. Finite element modeling (FEM)

A high-resolution finite element (FE) head model of an adult Sprague Dawley was developed. The geometry of skull and brain was based on the MicroCT images, T2-weighted MRI images and the rat brain atlas. The FE rat head model consists of all essential anatomical structures including the scalp, sandwiched skull, dura, arachnoid-pia, CSF, olfactory, cortex, corpus callosum, hippocampus, cerebellum, ventricles, brainstem with pyramidal tract, medial lemniscus and facial flesh. The rat head model was meshed with over 770,000 elements at resolution of 0.1–0.2 mm. The tie-break contact interface was defined between the arachnoid and the dura mater to simulate the potential sliding of the brain with respect to the skull in the subdural space. The brain response of the model was validated against nine dynamic cortical displacement measurements from in vivo experiments (Shreiber et al., 1999). In order to explore the localized mechanical response in the subregions of the hippocampus, the resolution of the whole brain model was refined to an average element size at 50 μm to explicitly represent the CA3, dentate gyrus, and CA1/CA2 and surrounding cortical and subcortical regions and structures. The total number of hexahedral elements meshed for the brain was increased from 220,000 to 2,400,000 of which 140,000 elements were meshed for the hippocampus (Fig. 1). Hypermesh (Altair Engineering, Troy, MI), Morpher (DEP, Troy, MI) and Hexmesher (DEP, Troy, MI) were used for the FE mesh development.

A viscoelastic, nearly incompressible material model was used to simulate mechanical behaviors of the brain tissue, cerebral spinal fluid, and pia-arachnoid membranes under large deformation. The heterogeneity of the brain tissue mechanical properties was reported for the hippocampal subregions (CA1, CA3 and dentate gyrus) and cortical layers (Gefen et al., 2003, Elkin et al., 2007, Elkin et al., 2010) and assigned to the corresponding regions of the refined FE model (Table 1). The material properties for other brain tissues and regions were based on published data (Zhang et al., 2001, Gefen et al., 2003, Mao et al., 2013). The differences in mechanical properties between different regions may help to understand the heterogeneous strain fields in hippocampus and cortex and to correlate with the observed pattern of membrane permeability alteration and cell death following in vivo CCI injury.

The CCI simulation was performed at the same condition as used in

Table 1
Material properties used in the finite element model for the various brain tissues and subregions.

Viscoelastic material	Shear modulus – short term, G_0 (kPa)	Shear modulus – long term, G_i (kPa)
White matter	2.5	0.88
Gray matter/cortex	2.8	0.84
Hippocampus, CA1	3.6	0.72
Hippocampus, CA3	3.3	0.66
Hippocampus, DG	2.9	0.58

vivo. The skull mesh was removed to simulate the 6.0 mm diameter craniectomy. The impactor was angled at 15° from vertical and was given a constant velocity of 3 m/s velocity impacting into the cortex to 2 mm depth and held for 250 ms. The maximum principal strain (true strain) in the cortex and hippocampus and the maximum shear stress within hippocampal subregions were computed and their magnitudes and patterns were correlated to the positive cells quantified by permeability markers. A nonlinear, dynamic explicit FE solver LS-DYNA (MPP R8.1.0 version) (Livermore Software Technology Corporation (LSTC), CA) was used for all FE simulations. LS-PrePost software (LSTC) was used for post-processing the model output results.

3. Results

3.1. Description of cells with acute plasma membrane disruption in the injured brain

We used a dye exclusion assay to analyze the extent of nonspecific membrane disruptions following a CCI in the rat in which an impermeant marker is introduced to the extracellular space and can only enter cells with a compromised plasma membrane (LaPlaca et al., 2009). Marker was distributed in brains by 2 h post-injection in naïve brains (data not shown). The general patterns of dye uptake was similar in all regions for both markers in injured brains, except the CA3 region of hippocampus, which took up Lucifer yellow (457 Da) more than dextran (3 kDa). Superficial layers of the cortex exhibited significantly more permeable cells than deeper cortex or striatum. Cellular uptake of the permeability marker was heterogeneous, with permeable cells appearing adjacent to non-permeable cells and different fluorescence intensities among permeable cells. Cells containing the highest levels of permeability presented a distinct shrunken morphology when compared with unaffected neighboring cells (Fig. 2). The morphology of permeable cells combined with immunostaining for NeuN revealed that cells that exhibited permeability marker uptake were primarily neurons (Fig. 3A–F). No astrocytes were observed with permeability marker (Fig. 3G, H).

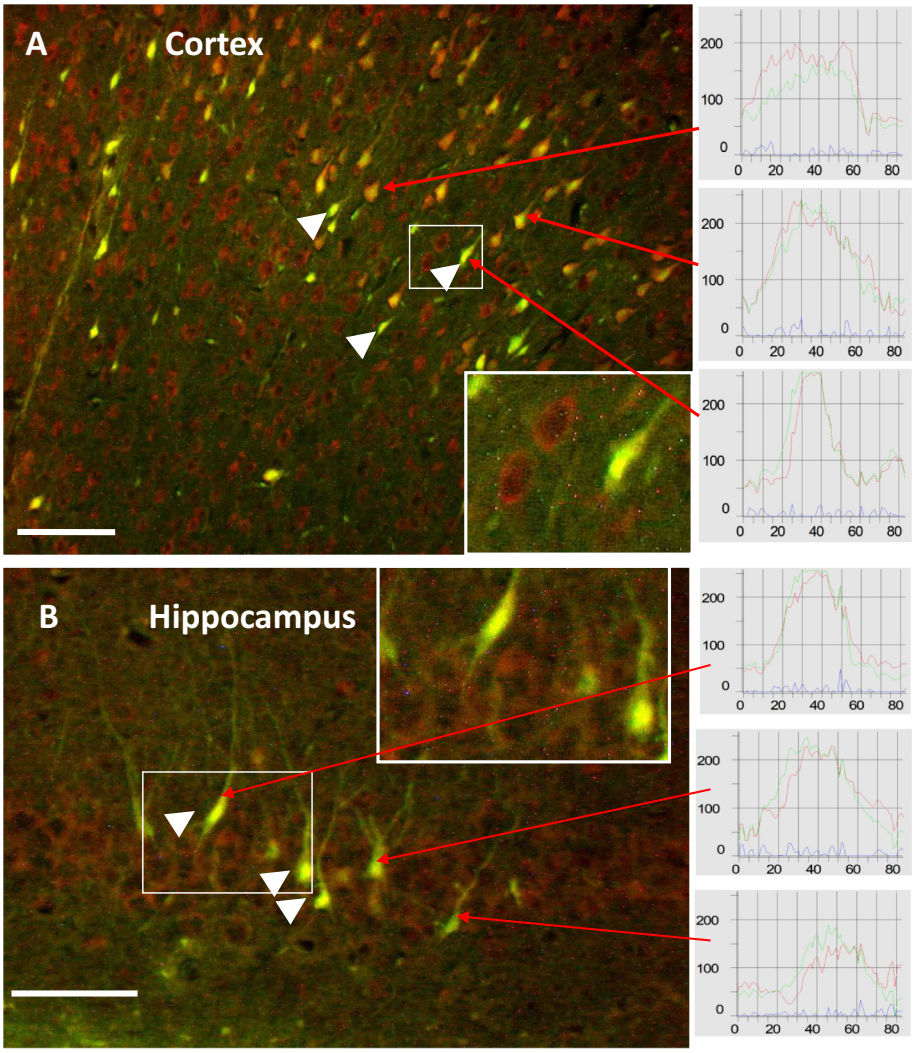

Fig. 2. Permeability patterns and cell morphology in the injured cortex and hippocampus. Representative permeability patterns in A) Cerebral cortex. B) CA3 subregion of the hippocampus. Permeable cells show differential uptake of the Lucifer yellow marker (yellow). Red arrows denote cells with different amount of dye uptake as depicted in the fluorescent intensity histograms on the right. X-axis in histograms denotes length of line profile used to evaluate intensity. Y-axis denotes pixel intensity values (0–255). Insets show magnified areas of interest. Note that the cells containing highest concentrations of Lucifer yellow present an exaggerated shrunken and elongated morphology (arrowheads). FluoroNissl (red) was used as a counterstain. Scale bar = 50 μm. (For interpretation of the references to color in this figure legend, the reader is referred to the web version of this article.)

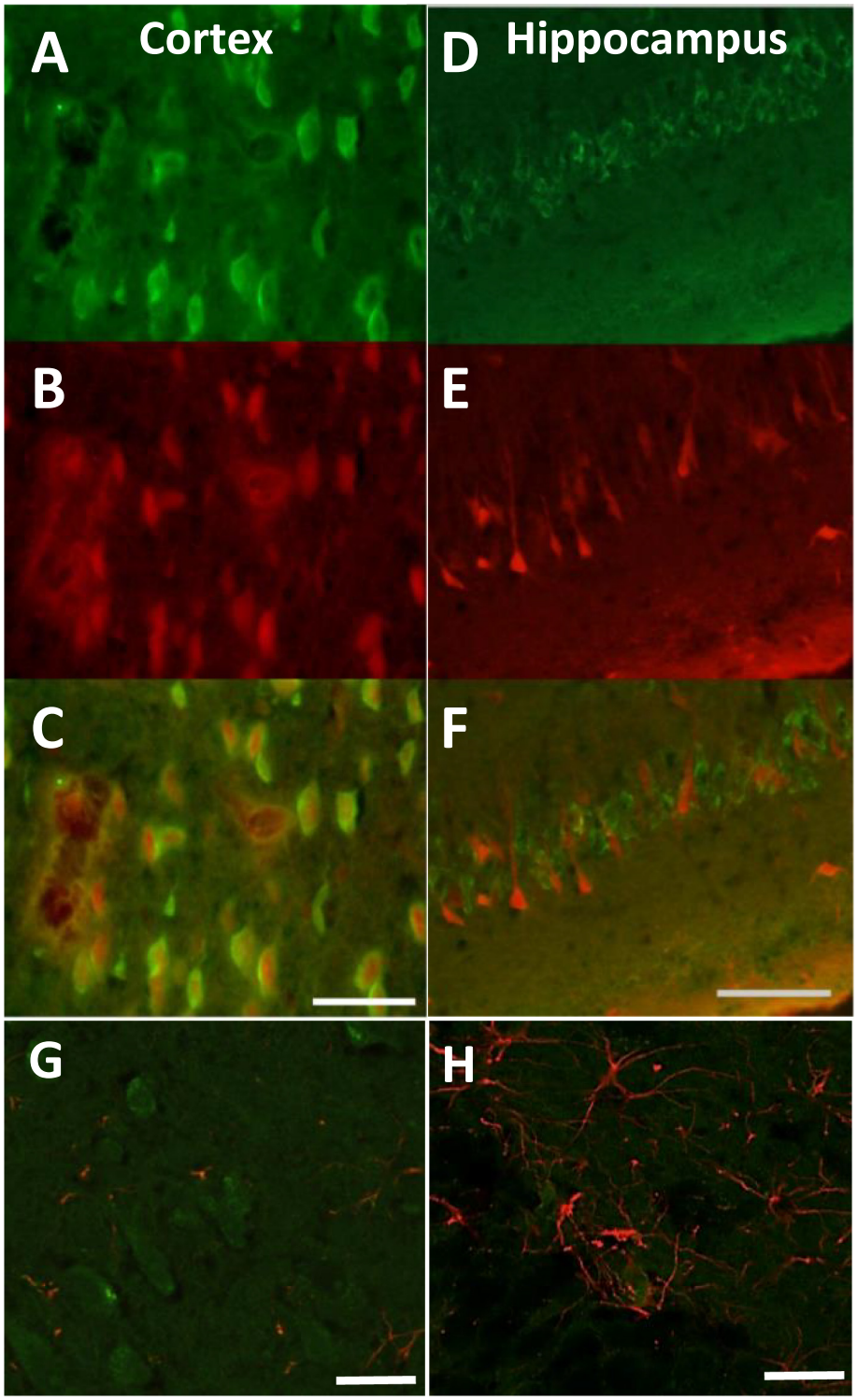

Fig. 3. Phenotype of permeable cells in the injured cortex and hippocampus. Proximal to the site of injury in the cortex 10 min following injury, neuronal nuclei were identified with NeuN immunostaining (green, A) and permeable cells identified by marker uptake (3 kD dextran, red, B). An overlay of the images reveals that the large majority of permeable cells in the cortex are neurons (C). Scale bar (A–C) = 50 μm). In the CA3 subregion of the hippocampus 10 min following injury, neuronal nuclei were identified with NeuN staining (green, D) and permeable cells identified by marker uptake (red, E). Permeable cells have a distinct neuronal morphology and stain positive for NeuN (F). Scale bar (D–F) = 100 μm. Astrocytes were identified by glial fibrillary acidic protein (GFAP) immunostaining 24 h following injury (GFAP, red; Lucifer yellow permeability dye, green) in the cortex (G) and hippocampus (H). We did not observe overlap in permeable cells and GFAP + astrocytes. Scale bar (G,H) = 50 μm. (For interpretation of the references to color in this figure legend, the reader is referred to the web version of this article.)

3.2. Distribution of mechanoporated cells in the injured brain

Plasma membrane damage was evident 10 min post-injury predominantly in the ipsilateral cortex and CA3 and dentate gyrus subregions of the hippocampus (Fig. 4A–F). Contralateral regions of injured brains contained relatively fewer permeable cells (Fig. 4G–L). Permeable cells in the hippocampus were clustered in high densities within the CA3 and dentate gyrus subregions, while fewer cells were located in sham brains (Fig. 4M, N). When comparing ipsilateral and contralateral sides, there was significantly higher percentage of positive cells in the ipsilateral CA3 and dentate gyrus regions of the hippocampal formation and the superficial layers of the ipsilateral cortex compared to their contralateral counterparts ($P < 0.05$) (Fig. 5A). Moreover, these regions had significantly more permeable cells compared to CA1, deep cortex, and striatum on the ipsilateral side ($P < 0.05$) (Fig. 5A).

3.3. Stress and strain patterns in the injured brain during impact

The maximum principal strain and maximum shear stress response-

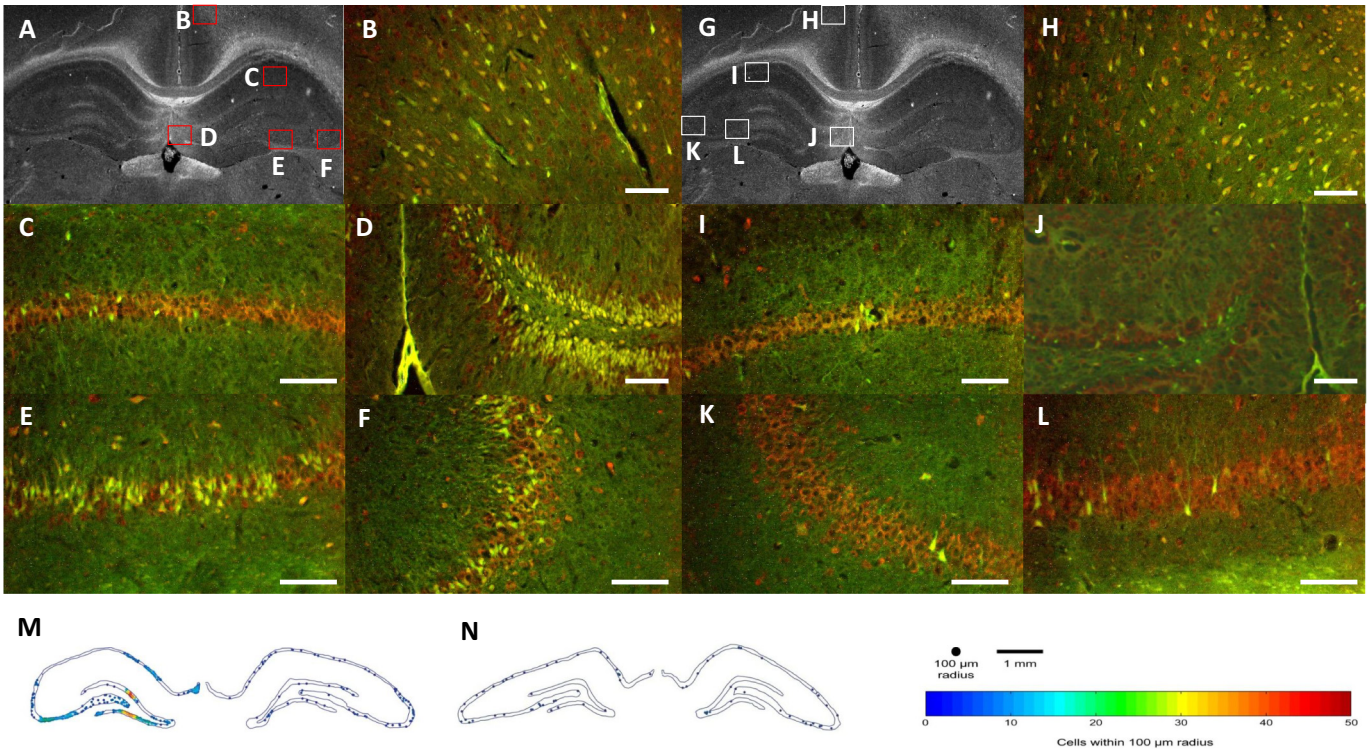

Fig. 4. Permeable cell distribution within the injured brain. Representative images from ipsilateral regions (A–F) and contralateral regions (G–L) of the cortex and hippocampus 10 min following CCI injury (permeable cells, Lucifer yellow; FluoroNissl counterstain, red). A) Low magnification bright field micrograph shows where subsequent photomicrographs were taken on the ipsilateral side (red boxes). B) Cerebral cortex presented a heterogeneous uptake pattern. C) Hippocampal CA1 region contained the lowest number of positive cells. D) In contrast, the dentate gyrus presented a comparatively high number of positive cells. E, F) The CA3 region also contained affected cells. G) Low magnification bright field micrograph shows where subsequent photographs were taken on the contralateral side (white boxes). H) Region of the cortex presented a heterogeneous uptake pattern. I) As in the ipsilateral side, hippocampal CA1 region contained few positive cells. J) The contralateral dentate gyrus presented few positive cells. K, L) The CA3 region contralateral to the injury presented few positive cells. The Cartesian coordinates of the locations of permeable cells in the cell body layers of the hippocampus of injured and sham brains were collected and plotted. Each point represents the location of a permeable cell, and the color of the point represents the density of permeable cells within a 100 µm radius. Representative hippocampi (located at approximately bregma −3.3 mm) are shown for injured (M) and sham (N) brains. Scale bars = 50 µm. (For interpretation of the references to color in this figure legend, the reader is referred to the web version of this article.)

time histories calculated by the FE model in the cortex, corpus callosum, hippocampus including the subregions in the areas under the impactor as well as on the contralateral side were analyzed. The strain and stress showed localized response patterns within the hippocampal subregions and cortex. The peak maximum principal strain (true strain) were compared between the hippocampus and the cortex regions where the percentage of positive cells was counted by permeability marker on both ipsilateral and contralateral sides. On the ipsilateral side, the highest strain was found in the superficial cortex (0.43). For the hippocampus, the peak strain was 0.36 in CA3 followed by 0.29 in the DG and 0.33 in the CA1/CA2 regions. The strain in the deep cortex and striatum regions (0.05) was much lower than that of the hippocampal region and superficial cortex (Fig. 5B). On the contralateral side, the strains in the upper cortex, CA3, dentate gyrus and CA1/CA2 were also higher than those in the lower cortex and striatum regions, similar to the strain localization pattern on the ipsilateral side. The strain magnitude in the upper cortex and hippocampus of the contralateral side was significantly lower than their counterparts from the ipsilateral side. The regional brain strain response patterns (Fig. 5C) significantly correlated to the spatial patterns of membrane damage ($r = 0.723$, CI, 0.256–0.917, $P = 0.007$, Fig. 5D).

3.4. Hippocampal acute membrane permeability and mechanical response

We focused on the hippocampus as a vulnerable brain region. We isolated the hippocampus using slice cultures and delivered a prescribed stretch. Across the hippocampus there was significant increases in membrane permeability for both 0.50 and 0.75 strain levels, but there was no difference between the two injury levels. Permeability in the CA3, CA4, and dentate gyrus increased significantly with 0.50 and 0.75 strain compared to control (unstretched) cultures (Fig. 6). CA1 contained significantly more permeable cells than control, but cultures stretched at 0.75 exhibited no significant increase in CA1. The maximum principal strain in the hippocampus (0.29–0.36) was lower than the stretch levels delivered to the cultures (0.50, 0.75) (see Fig. 5B). The peak maximum shear stress predicted in the CA1, CA3 and DG hippocampal subregions on the ipsilateral side is shown in Fig. 7A and the stress contour map is shown in Fig. 7B. The shear stress in the CA3 region (390 Pa) was slightly higher than that of DG region (350 Pa), consistent with the permeability patterns in both the injured brains and stretched slices. The shear stress in CA1 was approximately 50% lower than that of the CA3 region. The shear stress at the contralateral side was about 23% lower than of the ipsilateral side for the hippocampus region. This difference was much less than the difference predicted by the strain responses.

3.5. Prolonged plasmalemmal membrane damage correlates to cell degeneration

Although the permeability marker was introduced into the CSF 2 h before injury, many cells still contained permeability marker 24 h post-injury (Fig. 8C,D). Whereas the intracellular presence of permeability marker at 10 min was very clearly observed within both the somata and neurites of cells, by 24 h the permeability marker appeared punctuate in

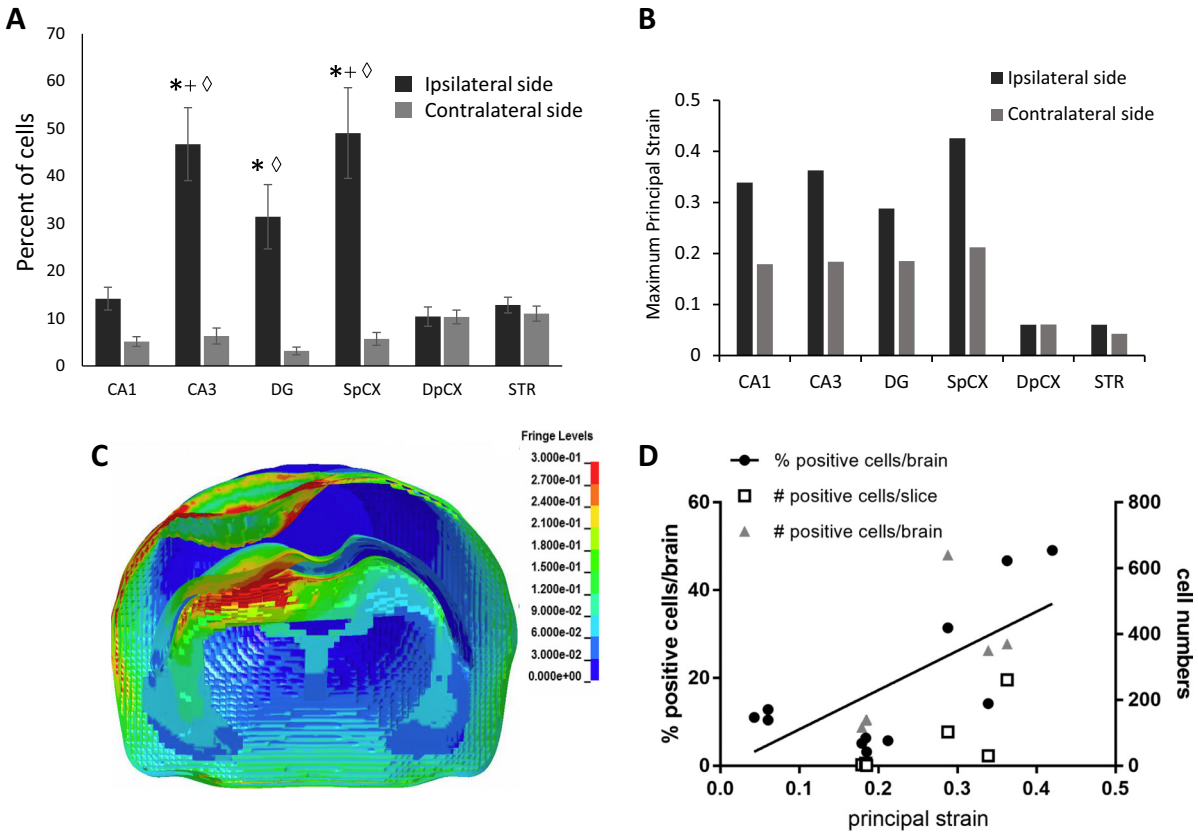

Fig. 5. Quantification of plasmalemmal damage and correlation with strain. There is a significantly higher percentage of cells permeable to Lucifer yellow on the ipsilateral hippocampal CA3 and dentate gyrus regions, and the superficial cortex (A) compared to the contralateral side (B) (*$P < 0.05$). Furthermore, these regions have a significantly higher percentage of positive cells compared to other brain regions assessed on the ipsilateral side ($^{+}P < 0.05$ vs. CA1/CA2; $^{\Diamond}P < 0.05$ vs. deep cortex and striatum). C) FE model predicted strain during impact. D) There was a significant correlation between cells positive for permeability marker and principal strain ($r = 0.723$, CI, 0.256–0.917, $P = 0.007$). (For interpretation of the references to color in this figure legend, the reader is referred to the web version of this article.)

and around cells (see Fig. 10A,D). With the exception of the contralateral CA1/CA2 and dentate gyrus subregions, there were more permeable cells in all hippocampal subregions compared to shams at 24 h post-injury ($P < 0.05$) (Fig. 8). Additionally the number of permeable cells in the CA3 subregion of the contralateral hippocampus in injured brains increased significantly compared to the ipsilateral CA3 subregion as well as the other contralateral subregions at 24 h ($P < 0.05$) (Fig. 8C). Sham brains contained few permeable cells (Fig. 8 B,D).

Quantification of Fluoro-Jade stained cells revealed statistically more cells in the CA1/CA2 and dentate gyrus subregions of the ipsilateral hippocampus at 10 min post-injury compared to the same subregions in shams ($P < 0.05$) (Fig. 9A, B). With the exception of the contralateral CA1/CA2 subregion, the increase in the number of Fluoro-Jade stained cells on both sides of the injured hippocampus compared to shams at 24 h was significant ($P < 0.05$) (Fig. 9C, D). There were also more Fluoro-Jade stained cells in the contralateral CA3 subregion compared to the CA1/CA2 subregion at 24 h. Faint Fluoro-Jade staining was present in a few cells in the hippocampus 10 min post-injury (Fig. 10A–C). However Fluoro-Jade staining was greatly increased 24 h post-injury, indicating neuronal degeneration, and Fluoro-Jade stained cells were easily distinguished from background (Fig. 10D–F). Few cells stained with Fluoro-Jade in sham animals.

Permeability marker and Fluoro-Jade staining overlapped in many cells, and this was especially evident at 24 h post-injury (Fig. 10F). Most cells that were Fluoro-Jade positive also contained permeability marker; however only a subset of cells containing permeability marker also exhibited Fluoro-Jade staining. Within the injured brain the percentage of permeable cells that also stained with Fluoro-Jade (Dextran with Fluoro-Jade) was only statistically increased in the contralateral hippocampus at 24 h compared to 10 min ($P < 0.05$) (Fig. 10G). These averages also suggest that by 24 h post-injury less than half of all permeable cells show signs of degeneration. Comparing all Fluoro-Jade stained cells, a greater percentage contained dextran (Fluoro-Jade with Dextran) at 10 min in the ipsilateral hippocampus compared to the contralateral hippocampus($P < 0.05$) (Fig. 10H). At 24 h post-injury most Fluoro-Jade stained cells also contained permeability marker.

4. Discussion

Plasma membrane damage was measured in the rat brain following a CCI injury and compared to the stress and strain patterns in a FEM model. It was postulated that membrane disruption during the insult is due to the strain at the tissue level. Plasma membrane permeability was evident in neurons in the cortex and hippocampus in a heterogeneous pattern, especially among hippocampal subregions. In both the cortex and hippocampus the vast majority of the cells were identified to be neuronal, based on NeuN immunostaining and morphology. The elongated cell body of permeable cells is consistent with pathomorphological features seen in injured neurons (Chen et al., 2003; Dunn-Meynell and Levin, 1997). GFAP positive cells did not overlap with permeable cells, consistent with other reports (Farkas et al., 2006; Whalen et al., 2008), although we cannot rule out a small percentage of nonneuronal damage. The brain areas with high numbers of permeable cells corresponded well with maximal principal strain, suggesting that mechanical

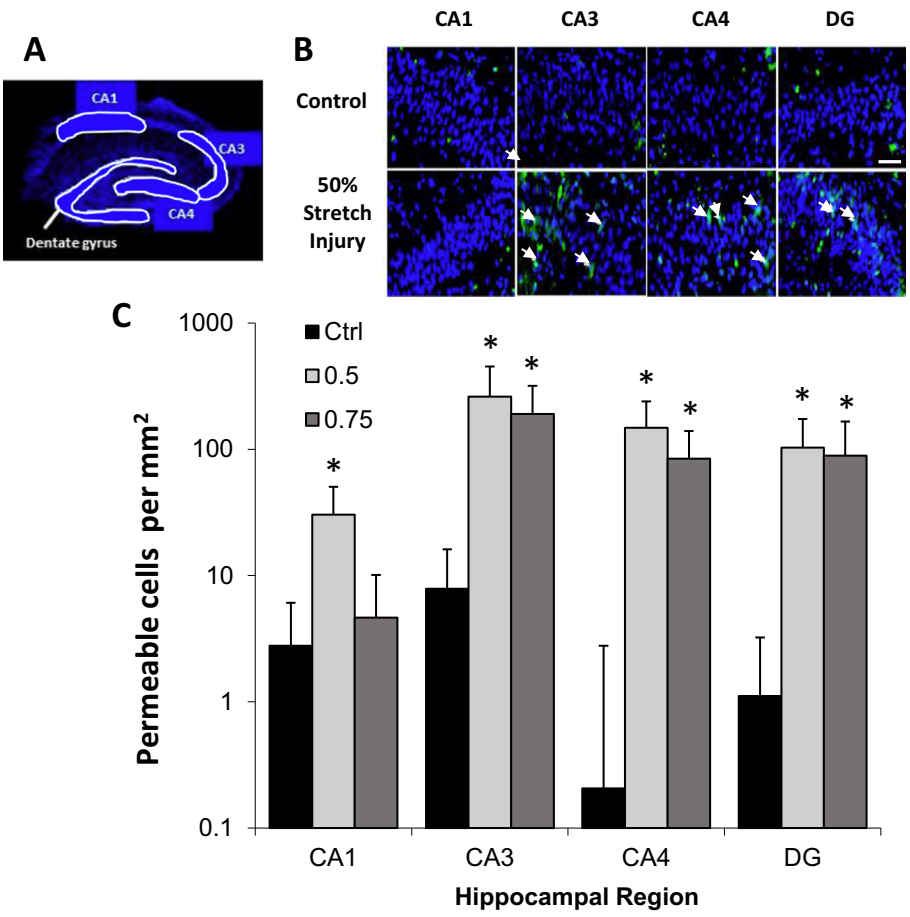

Fig. 6. Permeability following stretch injury in hippocampal organotypic cultures. A) Schematic of analyzed regions in organotypic culture (Hoechst positive nuclei in blue). B) Representative images show permeability marker uptake for control and 50% stretch-injured hippocampal organogypic cultures. Alexa positive cells are shown in green and Hoechst positive nuclei are shown in blue. Arrows indicate positively permeabilized cells. Increased uptake is evident in the stretch injured cultures, compared to control slices. Scale bar = 50 μm. C) Normalized Alexa positive cells across hippocampal subregions for control, 50% or 75% stretch. Immediate Alexa uptake increases significantly in CA3, CA4, and dentate gyrus for both stretch levels, compared to control. $^{*}P < 0.05$ compared to control cultures. (For interpretation of the references to color in this figure legend, the reader is referred to the web version of this article.)

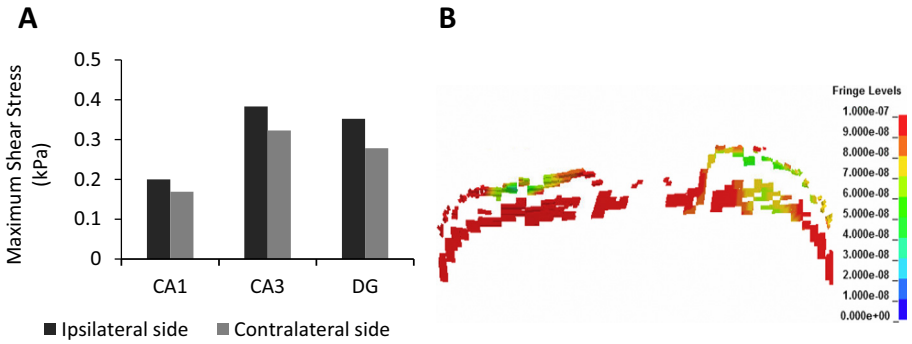

Fig. 7. Predicted shear stress in hippocampus. A) FE model predicted peak maximum shear stress responses within the hippocampal subregions on the ipsilateral and contralateral sides. B) FE model predicted shear stress contour on the hippocampal subregions. Fringe levels are shown in GPa.

responses contributes, in part, to the plasmalemmal damage seen immediately following TBI.

Strain-induced permeability changes are supported by a number of studies that examine the relationship between mechanical loading and primary cell membrane damage. Neural cell and tissue preparations have been shown to have strain and strain rate dependence for mechanoporation (Cullen et al., 2011; Geddes et al., 2003a, 2003b; Geddes-Klein et al., 2006; LaPlaca et al., 1997; Shi and Whitebone, 2006). Increased cortical impact depth in a mouse model of TBI was associated with more permeable cells in the hippocampus (Whalen et al., 2008), further supporting that higher loading magnitude results in more acute membrane damage. In non-neuronal cells subjects to loading, strain and strain rate have also been shown to correlate to membrane permeability changes (Salvador et al., 2015; Slomka and Gefen, 2012; Stroetz et al., 2001; Vlahakis et al., 2002). Interestingly, in a recent report using bulk strain rates in compression injury to 3D neural cultures acute mechanoporation was not prevalent (Bar-Kochba et al., 2016). This could be due to the difference in primary loading modality. In the current study we stretched organotypic culture, an ex vivo preparation that benefits from having intact tissue, perhaps transducing the stress more directly to the cells. In a 2011 study by Cullen et al. (Cullen et al., 2011), significant mechanoporation under shear loading, while in the same study when 3D cultures were subject to compression at the same strains and strain rates relatively less membrane compromise was observed, consistent with the Bar-Kochba et al. report (Bar-Kochba et al., 2016). Furthermore, the local strains calculated in the latter study were nearly half those estimated by the FEM, albeit the length scales are not the same. These studies point to a possible heterogeneous mechanical threshold among cells and also underline the need to better understand the relationship between bulk

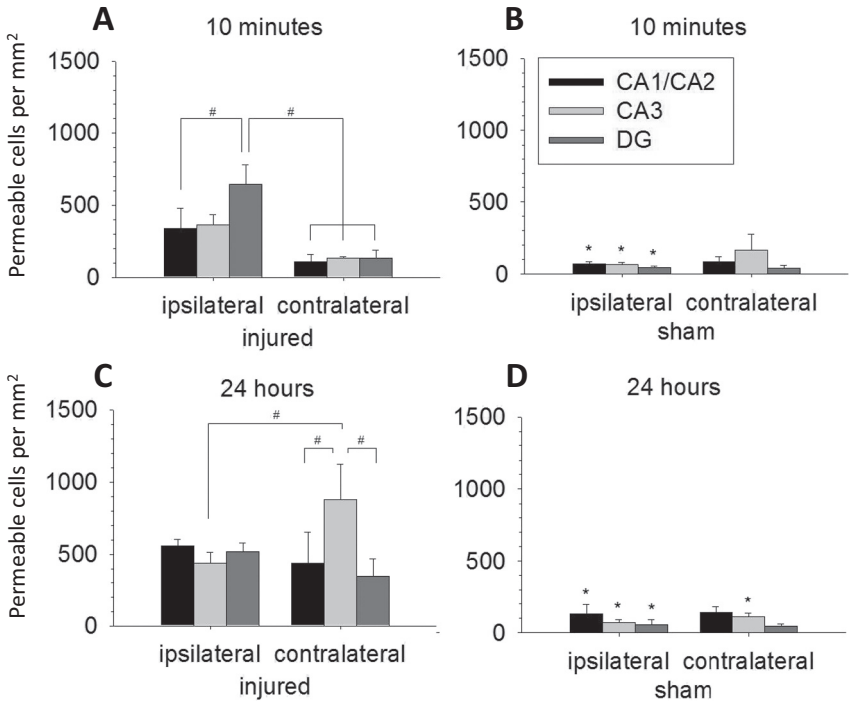

Fig. 8. Plasma membrane permeability increases in the hippocampus 10 min and 24 h following injury. Cells in the pyramidal (CA1/CA2 and CA3 subregions) and granule (dentate gyrus (DG) subregion) cell body layers of the hippocampus were examined for the presence of permeability marker (3 kD dextran). At 10 min post-surgery, more permeable cells were identified in the ipsilateral hippocampus in injured animals compared to the contralateral hippocampus (A) as well as compared to the ipsilateral hippocampus in sham animals (B). At 24 h post injury, the ipsilateral and contralateral hippocampi in injured animals contained significantly more permeable cells (C) than the same regions in sham animals (D). In addition, the contralateral hippocampus in injured animals exhibited a significant increase in the number of permeable cells from 10 min to 24 h post-surgery. Data graphed as mean (standard error of the mean) ($^{*}P < 0.05$ compared to injured, $^{\#}P < 0.05$ as indicated).

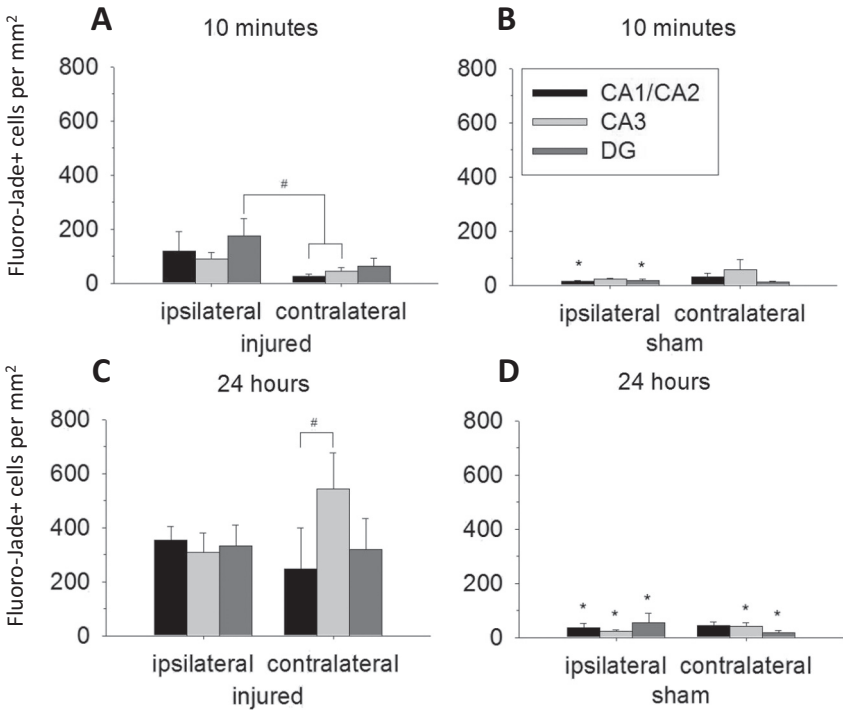

Fig. 9. Cell death increases in the hippocampus following injury. Fluoro-Jade staining was used to identify degenerating neurons in the cell body layers of the hippocampus following injury. Few Fluoro-Jade positive cells were identified in sham animals. At 10 min post-injury, significantly more Fluoro-Jade positive cells were identified in the ipsilateral hippocampus of injured animals compared to the contralateral hippocampus in injured animals (A) as well as compared to the ipsilateral hippocampus in sham animals (B). At 24 h post injury, both the ipsilateral and contralateral hippocampi in injured animals contained significantly more Fluoro-Jade positive cells (C) than the same regions in sham animals (D). In addition, the contralateral and ipsilateral hippocampi in injured animals exhibited a significant increase in the number of permeable cells in the same regions from 10 min (A)to 24 h (C) post-surgery. Data graphed as mean (standard error of the mean) ($^{*}P < 0.05$ compared to injured, $^{\#}P < 0.05$ as indicated).

loading conditions to strain at the cell level and subsequent acute response.

The spatial patterns of the peak maximum principal strain predicted by the model in CA3, DG subregions and cortex showed reasonable correlations with the spatial profile of quantified positive cells (Fig. 5A), suggesting a relationship between mechanical loading and mechanoporation. Although compressive strain in the CA1 was in the same range as other hippocampal subregions, the mechanoporation levels were lower, exhibiting relative poor correlation. This observation is consistent with a recent study in which compressive strain did not correlate with mechanoporation (Bar-Kochba et al., 2016), suggesting that compressive strain may not be a dominant factor in traumatic membrane failure. Many factors might explain the disparity seen in the present study, including cellular orientation, inherent cell differences, and dominant mechanical factors. For example, the maximum shear stress or shear strain (proportion to the stress) experienced by the CA1 region was found to be much lower than the CA3 and DG subregions, consistent with the membrane damage patterns. The model predictions implied that the combined localized maximum principal strain and deviatoric stress may be the relevant local loadings involved in inducing acute mechanoporation damage in the current CCI model. Cell process orientation and cell-cell and cell-extracellular matrix

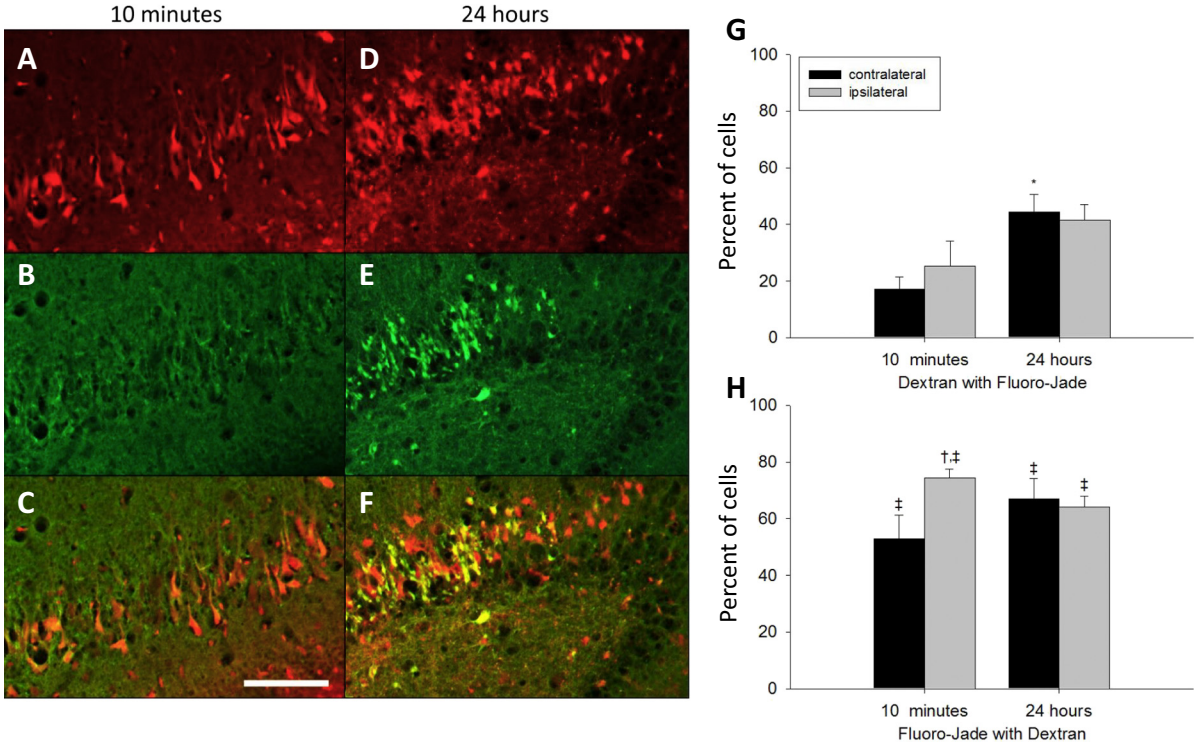

Fig. 10. Plasma membrane permeability and cell death in the hippocampus at 10 min and 24 h post-injury. Permeability marker uptake (A, D) indicates which cells in the CA3 (A–C) and dentate gyrus (D–F) subregions of the ipsilateral hippocampus sustained plasma membrane damage by the mechanical insult. Fluoro-Jade staining shows degenerating neurons in the same tissue sections at 10 min (B) and 24 h (C) post-injury, with more intense Fluoro-Jade staining evident at the later time point. Overlays of these photomicrographs (C, F) reveals nearly complete colocalization of Fluoro-Jade staining with permeability marker uptake, whereas only a subset of permeable cells are Fluoro-Jade positive (scale bar = 100 μm). In injured brains few permeable cells at 10 min post-injury were also Fluoro-Jade positive, while slightly more permeable cells at 24 h post-injury were Fluro-Jade positive (G, Dextran with Fluoro-Jade). However, a larger portion of Fluoro-Jade positive cells also contained dextran (H, Fluoro-Jade with dextran). ($^{*}P < 0.05$ compared to 10 min, $^{\dagger}P < 0.05$ compared to contralateral, $^{\ddagger}P < 0.05$ compared to Dextran with Fluoro-Jade) (mean (standard error of the mean)).

interactions may contribute to the heterogeneous mechanoporation response and cannot be captured under the current the computer simulation parameters.

Different levels of injury likely occur within the brain depending on distance from impact, cell orientation/organization, and mechanical properties. Injury heterogeneity is evident in the current study by the variable levels of marker intensity and the different uptake patterns depending on marker size. Among permeable cells different fluorescent intensities of permeability marker were observed, suggesting different levels of injury within a region. Plasma membrane damage and repair is a dynamic process (Cooper and McNeil, 2015). Cells with primary mechanoporation may have membrane damage that reseals quickly, catastrophic injury in which no dye is trapped, or remain leaky.

Given the largely similar patterns of mechanoporation in the brain using three different markers in two different injury models, we suggest that mechanically induced membrane defects include pores in the nanometer range, based on equivalent Stokes' radii of the markers used in this study. At the nanoscale the threshold for nonspecific pore initiation in lipid bilayers was predicted using molecular dynamics simulation where initial pore formation occurred at a range of strains (0.12–0.41) with a critical size (1 nm) defect formed consistently above 0.70 strain (Murphy et al., 2016). This implies that small pores are not stable and that significant molecular level strains are necessary for membrane breach, possibly partially explaining why mechanoporation was not observed in 3D cell culture undergoing compression and estimated to have axial shear strain and compressive axial strain < 0.20 (Bar-Kochba et al., 2016). It is also not known what the threshold for membrane damage in terms of bulk strain and strain rate. In our in vitro model of stretch we observed nearly the same level of mechanoporation for 50% and 75%, suggesting that a threshold was reached before 50%. It will be important in future studies to directly compare a large range of strain and strain rate and compare acute response as well as attempt to estimate local strains. In our study the CA3 subregion showed higher permeability levels when the smaller markers were used (Alexa, 570 Da, and Lucifer yellow, 457 Da), suggesting a lower threshold for mechanoporation. This is consistent with another study in which CA3 and hilar region of the dentate gyrus show greater membrane permeability than CA1 after TBI (Singleton and Povlishock, 2004). In fact, the CA3 region exhibited higher tensile strains compared to CA1 in a high resolution FEM of CCI (Mao et al., 2013), supporting the inference that higher strains correlate to membrane damage. This is at least partially due to the mechanical properties of the hippocampus, in which the CA1 subregion is stiffer than both the CA3 and dentate gyrus subregions (Elkin et al., 2011). Hippocampus cell loss has been observed in many TBI models (Anderson et al., 2005; Colicos et al., 1996; Grady et al., 2003; Hall et al., 2008; Hicks et al., 1996; Sato et al., 2001), likely due to a combination of functional and mechanical properties (Kotapka et al., 1991; Lowenstein et al., 1992; Mao et al., 2013). Patterns of hippocampal damage in parasagittal CCI have been shown to be similar to the mechanoporation distribution shown here with preferential cell death in CA3 and dentate gyrus subregions (Anderson et al., 2005; Grady et al., 2003; Saatman et al., 2006; Smith et al., 1995).

There is evidence that in addition to mechanoporation at the time of injury, delayed onset membrane permeability occurs following TBI (Farkas et al., 2006), pointing to a combination of primary and secondary mechanisms. Delayed membrane permeability may be due to reactive oxygen species and/or gradual cell death (Hall, 2015).Interestingly, we observed delayed permeability and cell death on both the ipsilateral and contralateral sides. Strains and stresses distant from the impact side are notably less than those directly below the primary

injury site, however they may still be of significance. Contralateral damage is evident in experimental models of TBI both acutely and chronically (e.g., (Glushakova et al., 2014, Pischiutta et al., 2018, Smith et al., 1994, Tran et al., 2006)).

A correlation between degenerating cells and permeable cells has been observed in CCI (Whalen et al., 2008). We found that most degenerating neurons in the hippocampus exhibited plasma membrane damage. However, only a subset of neurons in the hippocampus with plasma membrane damage showed evidence of degeneration. While other factors likely contribute to neuronal outcome, thus study suggests there may exist local differences in susceptibility to plasma membrane damage and that plasma membrane damage may be a critical factor in determining neuronal survival following TBI.

Further evidence that membrane damage is detrimental to cell survival is evident when membrane resealing agents are administered following injury, suggesting that prevention of plasma membrane damage may be a possible therapeutic target (Jin, 2014). Polyethylene glycol (PEG) treatment has been shown to reseal membranes, restore function, and spare cells in both spinal cord injury (Cho et al., 2010; Luo et al., 2002; Shi and Borgens, 1999; Shi and Borgens, 2000) and TBI (Koob et al., 2005; Koob et al., 2008). In vitro delivery of the membrane stabilizer Poloxamer-188 reduced membrane damage and limited cell death after mechanical cell injury (Kilinc et al., 2007; Kilinc et al., 2008; Luo et al., 2013; Serbest et al., 2005; Serbest et al., 2006). However, despite the observation that membrane resealing with Kollidon VA64 resulted in improved outcome in injured rats (Mbye et al., 2012) and increased conduction in damage white matter (Ping et al., 2014) it was shown not to reduce membrane damage following experimental TBI (Ping et al., 2014), suggesting that membrane repair is not sufficient to prevent ongoing pathology.

5. Conclusions

In conclusion, we show that an experimental model of TBI exhibits mechanoporation and cell death that correlates to maximum principal strain and maximum shear stress estimated by a high resolution finite element model. Disruptions of the neuronal plasmalemma are likely part of the primary insult and depend on cell mechanical properties, tissue organization, and distance from the contusion site. Membrane damage can trigger numerous detrimental events by allowing molecules and ions that are normally only present extracellularly to enter the cell. Understanding the mechanisms of mechanically induced cell damage may identify therapeutic targets and enable improved predictions of injuries and outcomes after TBI.

Acknowledgements

The authors appreciate the technical support received from Dr. C.M. Simon and analysis assistance from C.K. Giardina. This work was funded by the Whitaker Foundation, the Institute for Bioengineering and Bioscience at the Georgia Institute of Technology.

References

Anderson, K.J., Miller, K.M., Fugaccia, I., Scheff, S.W., 2005. Regional distribution of Fluoro-Jade B staining in the hippocampus following traumatic brain injury. Exp. Neurol. 193 (1), 125–130.

Bar-Kochba, E., Scimone, M.T., Estrada, J.B., Franck, C., 2016. Strain and rate-dependent neuronal injury in a 3D in vitro compression model of traumatic brain injury. Sci. Rep. 6, 30550.

Bukhatwa, S., Iravani, M.M., Zeng, B.Y., Cooper, J.D., Rose, S., Jenner, P., 2009. An immunohistochemical and stereological analysis of PSI-induced nigral neuronal degeneration in the rat. J. Neurochem. 109 (1), 52–59.

Carbonell, W.S., Grady, M.S., 1999. Regional and temporal characterization of neuronal, glial, and axonal response after traumatic brain injury in the mouse. Acta Neuropathol. (Berl) 98 (4), 396–406.

Chen, S., Pickard, J., Harris, N., 2003. Time course of cellular pathology after controlled cortical impact injury. Exp. Neurol. 182 (1), 87–102.

Cho, A.M., Liu, J., Lam, C.K., Dvorak, M., Tetzlaff, W., Oxland, T.R., 2007. Contusion, dislocation, and distraction: primary hemorrhage and membrane permeability in distinct mechanisms of spinal cord injury. J. Neurosurg. Spine 6 (3), 255–266.

Cho, Y., Shi, R., Ivanisevic, A., Borgens, R.B., 2010. Functional silica nanoparticle-mediated neuronal membrane sealing following traumatic spinal cord injury. J. Neurosci. Res. 88 (7), 1433–1444.

Colicos, M.A., Dixon, C.E., Dash, P.K., 1996. Delayed, selective neuronal death following experimental cortical impact injury in rats: possible role in memory deficits. Brain Res. 739 (1–2), 111–119.

Cooper, S.T., McNeil, P.L., 2015. Membrane repair: mechanisms and pathophysiology. Physiol. Rev. 95 (4), 1205–1240.

Cullen, D.K., Vernekar, V.N., LaPlaca, M.C., 2011. Trauma-induced plasmalemma disruptions in three-dimensional neural cultures are dependent on strain modality and rate. J. Neurotrauma 28 (11), 2219–2233.

Davson, H., Hollingsworth, G., Segal, M.B., 1970. The mechanism of drainage of the cerebrospinal fluid. Brain 93 (4), 665–678.

De Simoni, A., My Yu, L., 2006. Preparation of organotypic hippocampal slice cultures: interface method. Nat. Protoc. 1, 1439.

Dixit, P., Liu, G., 2016. A review on recent development of finite element models for head injury simulations. Arch. Comput. Meth. Eng. 1–53.

Dunn-Meynell, A., Levin, B., 1997. Histological markers of neuronal, axonal and astrocytic changes after lateral rigid impact traumatic brain injury. Brain Res. 761 (1), 25–41.

Egert, U., Schlosshauer, B., Fennrich, S., Nisch, W., Fejtl, M., Knott, T., Müller, T., Hämmerle, H., 1998. A novel organotypic long-term culture of the rat hippocampus on substrate-integrated multielectrode arrays. Brain Res. Protocol. 2 (4), 229–242.

Elkin, B.S., Azeloglu, E.U., Costa, K.D., Morrison 3rd, B., 2007. Mechanical heterogeneity of the rat hippocampus measured by atomic force microscope indentation. J. Neurotrauma 24 (5), 812–822.

Elkin, B.S., Ilankovan, A., Morrison 3rd, B., 2010. Age-dependent regional mechanical properties of the rat hippocampus and cortex. J. Biomech. Eng. 132 (1), 011010.

Elkin, B.S., Ilankovan, A.I., Morrison, B., 2011. A detailed viscoelastic characterization of the P17 and adult rat brain. J. Neurotrauma 28 (11), 2235–2244.

Farkas, O., Lifshitz, J., Povlishock, J.T., 2006. Mechanoporation induced by diffuse traumatic brain injury: an irreversible or reversible response to injury? J. Neurosci. 26 (12), 3130–3140.

Gao, X., Deng, P., Xu, Z.C., Chen, J., 2011. Moderate traumatic brain injury causes acute dendritic and synaptic degeneration in the hippocampal dentate gyrus. PLoS One 6 (9), e24566.

Geddes, D.M., Cargill 2nd, R.S., LaPlaca, M.C., 2003a. Mechanical stretch to neurons results in a strain rate and magnitude-dependent increase in plasma membrane permeability. J. Neurotrauma 20 (10), 1039–1049.

Geddes, D.M., LaPlaca, M.C., Cargill 2nd, R.S., 2003b. Susceptibility of hippocampal neurons to mechanically induced injury. Exp. Neurol. 184 (1), 420–427.

Geddes-Klein, D.M., Schiffman, K.B., Meaney, D.F., 2006. Mechanisms and consequences of neuronal stretch injury in vitro differ with the model of trauma. J. Neurotrauma 23 (2), 193–204.

Gefen, A., Gefen, N., Zhu, Q., Raghupathi, R., Margulies, S., 2003. Age-dependent changes in material properites of the brain and braincase of the rat. J. Neurotrauma 20 (11), 1163–1177.

Glushakova, O.Y., Johnson, D., Hayes, R.L., 2014. Delayed increases in microvascular pathology after experimental traumatic brain injury are associated with prolonged inflammation, blood–brain barrier disruption, and progressive white matter damage. J. Neurotrauma 31 (13), 1180–1193.

Grady, M.S., Charleston, J.S., Maris, D., Witgen, B.M., Lifshitz, J., 2003. Neuronal and glial cell number in the hippocampus after experimental traumatic brain injury: analysis by stereological estimation. J. Neurotrauma 20 (10), 929–941.

Hall, E.D., 2015. The Contributing Role of Lipid Peroxidation and Protein Oxidation in the Course of CNS Injury Neurodegeneration and Neuroprotection: An Overview. Brain Neurotrauma: Molecular, Neuropsychological, and Rehabilitation Aspects. F. H. Kobeissy. Boca Raton (FL).

Hall, E.D., Bryant, Y.D., Cho, W., Sullivan, P.G., 2008. Evolution of post-traumatic neurodegeneration after controlled cortical impact traumatic brain injury in mice and rats as assessed by the de Olmos silver and fluorojade staining methods. J. Neurotrauma 25 (3), 235–247.

Hicks, R., Smith, D., Lowenstein, D., Marie, R.S., McIntosh, T., 1993. Mild experimental brain injury in the rat induces cognitive deficits associated with regional neuronal loss in the hippocampus. J. Neurotrauma 10 (4), 405–414.

Hicks, R., Soares, H., Smith, D., Mcintosh, T., 1996. Temporal and spatial characterization of neuronal injury following lateral fluid-percussion brain injury in the rat. Acta Neuropathol. 91 (3), 236–246.

Inman, C., Rees, L., Barker, E., Haverson, K., Stokes, C., Bailey, M., 2005. Validation of computer-assisted, pixel-based analysis of multiple-colour immunofluorescence histology. J. Immunol. Methods 302 (1), 156–167.

Jin, X., 2014. Membrane resealing as a promising strategy for early treatment of neurotrauma. Neural Regen. Res. 9 (21), 1876.

Kilinc, D., Gallo, G., Barbee, K., 2007. Poloxamer 188 reduces axonal beading following mechanical trauma to cultured neurons. In: Conf Proc IEEE Eng Med Biol Soc. 2007. pp. 5395–5398.

Kilinc, D., Gallo, G., Barbee, K.A., 2008. Mechanically-induced membrane poration causes axonal beading and localized cytoskeletal damage. Exp. Neurol. 212 (2), 422–430.

Kilinc, D., Gallo, G., Barbee, K.A., 2009. Mechanical membrane injury induces axonal beading through localized activation of calpain. Exp. Neurol. 219 (2), 553–561.

Kleiven, S., 2006. Evaluation of head injury criteria using a finite element model validated against experiments on localized brain motion, intracerebral acceleration, and intracranial pressure. Int. J. Crashworthiness 11 (1), 65–79.

Koob, A.O., Duerstock, B.S., Babbs, C.F., Sun, Y., Borgens, R.B., 2005. Intravenous

polyethylene glycol inhibits the loss of cerebral cells after brain injury. J. Neurotrauma 22 (10).
Koob, A.O., Colby, J.M., Borgens, R.B., 2008. Behavioral recovery from traumatic brain injury after membrane reconstruction using polyethylene glycol. J. Biol. Eng. 2 (1), 9.
Kotapka, M.J., Gennarelli, T.A., Graham, D.I., Adams, J.H., Thibault, L.E., Ross, D.T., Ford, I., 1991. Selective vulnerability of hippocampal neurons in acceleration-induced experimental head injury. J. Neurotrauma 8 (4), 247–258.
Laplaca, M.C., Lessing, M.C., 2012. Assessment of membrane permeability after traumatic brain injury. In: Animal Models of Acute Neurological Injuries II: Injury and Mechanistic Assessments. Vol. 2. pp. 275–298.
LaPlaca, M.C., Prado, G.R., 2010. Neural mechanobiology and neuronal vulnerability to traumatic loading. J. Biomech. 43 (1), 71–78.
LaPlaca, M.C., Lee, V.M., Thibault, L.E., 1997. An in vitro model of traumatic neuronal injury: loading rate-dependent changes in acute cytosolic calcium and lactate dehydrogenase release. J. Neurotrauma 14 (6), 355–368.
LaPlaca, M.C., Lessing, M.C., Prado, G.R., Simon, C.M., 2009. Susceptibility of Neuronal Membranes to Mechanical Injury and Implications for Repair.
Lowenstein, D., Thomas, M., Smith, D., McIntosh, T., 1992. Selective vulnerability of dentate hilar neurons following traumatic brain injury: a potential mechanistic link between head trauma and disorders of the hippocampus. J. Neurosci. 12 (12), 4846–4853.
Luo, J., Borgens, R., Shi, R., 2002. Polyethylene glycol immediately repairs neuronal membranes and inhibits free radical production after acute spinal cord injury. J. Neurochem. 83 (2), 471–480.
Luo, C.-L., Chen, X.-P., Li, L.-L., Li, Q.-Q., Li, B.-X., Xue, A.-M., Xu, H.-F., Dai, D.-K., Shen, Y.-W., Tao, L.-Y., 2013. Poloxamer 188 attenuates in vitro traumatic brain injury-induced mitochondrial and lysosomal membrane permeabilization damage in cultured primary neurons. J. Neurotrauma 30 (7), 597–607.
Mao, H., Zhang, L., Yang, K.H., King, A.I., 2006. Application of a finite element model of the brain to study traumatic brain injury mechanisms in the rat. Stapp Car Crash J. 50, 583–600.
Mao, H., Elkin, B.S., Genthikatti, V.V., Morrison III, B., Yang, K.H., 2013. Why is CA3 more vulnerable than CA1 in experimental models of controlled cortical impact-induced brain injury? J. Neurotrauma 30 (17), 1521–1530.
Mbye, L.H., Keles, E., Tao, L., Zhang, J., Chung, J., Larvie, M., Koppula, R., Lo, E.H., Whalen, M.J., 2012. Kollidon VA64, a membrane-resealing agent, reduces histopathology and improves functional outcome after controlled cortical impact in mice. J. Cereb. Blood Flow Metab. 32 (3), 515–524.
Murphy, M., Horstemeyer, M., Gwaltney, S.R., Stone, T., LaPlaca, M., Liao, J., Williams, L., Prabhu, R., 2016. Nanomechanics of phospholipid bilayer failure under strip biaxial stretching using molecular dynamics. Model. Simul. Mater. Sci. Eng. 24 (5), 055008.
Okonkwo, D.O., Pettus, E.H., Moroi, J., Povlishock, J.T., 1998. Alteration of the neurofilament sidearm and its relation to neurofilament compaction occurring with traumatic axonal injury. Brain Res. 784 (1–2), 1–6.
Pettus, E.H., Povlishock, J.T., 1996. Characterization of a distinct set of intra-axonal ultrastructural changes associated with traumatically induced alteration in axolemmal permeability. Brain Res. 722 (1–2), 1–11.
Pettus, E.H., Christman, C.W., Giebel, M.L., Povlishock, J.T., 1994. Traumatically induced altered membrane permeability: its relationship to traumatically induced reactive axonal change. J. Neurotrauma 11 (5), 507–522.
Ping, X., Jiang, K., Lee, S.-Y., Cheng, J.-X., Jin, X., 2014. PEG-PDLLA micelle treatment improves axonal function of the corpus callosum following traumatic brain injury. J. Neurotrauma 31 (13), 1172–1179.
Pischiutta, F., Micotti, E., Hay, J.R., Marongiu, I., Sammali, E., Tolomeo, D., Vegliante, G., Stocchetti, N., Forloni, G., De Simoni, M.-G., 2018. Single severe traumatic brain injury produces progressive pathology with ongoing contralateral white matter damage one year after injury. Exp. Neurol. 300, 167–178.
Povlishock, J.T., Pettus, E.H., 1996. Traumatically induced axonal damage: evidence for enduring changes in axolemmal permeability with associated cytoskeletal change. Acta Neurochir. Suppl. 66, 81–86.
Raghupathi, R., McIntosh, T.K., 1996. Regionally and temporally distinct patterns of induction of *c-fos*, *c-jun* and junB mRNAs following experimental brain injury in the rat. Mol. Brain Res. 37, 134–144.
Rieselbach, R.E., Di Chiro, G., Freireich, E.J., Rall, D.P., 1962. Subarachnoid distribution of drugs after lumbar injection. N. Engl. J. Med. 267, 1273–1278.
Saatman, K.E., Feeko, K.J., Pape, R.L., Raghupathi, R., 2006. Differential behavioral and histopathological responses to graded cortical impact injury in mice. J. Neurotrauma 23 (8), 1241–1253.
Salvador, E., Burek, M., Förster, C.Y., 2015. Stretch and/or oxygen glucose deprivation (OGD) in an in vitro traumatic brain injury (TBI) model induces calcium alteration and inflammatory cascade. Front. Cell. Neurosci. 9.
Sato, M., Chang, E., Igarashi, T., Noble, L.J., 2001. Neuronal injury and loss after traumatic brain injury: time course and regional variability. Brain Res. 917 (1), 45–54.
Schmued, L.C., Hopkins, K.J., 2000. Fluoro-Jade B: a high affinity fluorescent marker for the localization of neuronal degeneration. Brain Res. 874 (2), 123–130.
Serbest, G., Horwitz, J., Barbee, K., 2005. The effect of poloxamer-188 on neuronal cell recovery from mechanical injury. J. Neurotrauma 22 (1), 119–132.
Serbest, G., Horwitz, J., Jost, M., Barbee, K., 2006. Mechanisms of cell death and neuroprotection by poloxamer 188 after mechanical trauma. FASEB J. 20 (2), 308–310.
Shi, R., Borgens, R.B., 1999. Acute repair of crushed guinea pig spinal cord by polyethylene glycol. J. Neurophysiol. 81 (5), 2406–2414.
Shi, R., Borgens, R.B., 2000. Anatomical repair of nerve membranes in crushed mammalian spinal cord with polyethylene glycol. J. Neurocytol. 29 (9), 633–643.
Shi, R., Whitebone, J., 2006. Conduction deficits and membrane disruption of spinal cord axons as a function of magnitude and rate of strain. J. Neurophysiol. 95 (6), 3384–3390.
Shreiber, D.I., Bain, A.C., Ross, D.T., Smith, D.H., Gennarelli, T.A., Mcintosh, T.K., Meaney, D.F., 1999. Experimental investigation of cerebral contusion: histopathological and immunohistochemical evaluation of dynamic cortical deformation. J. Neuropathol. Exp. Neurol. 58 (2), 153–164.
Simon, C.M., Sharif, S., Tan, R.P., Laplaca, M.C., 2009. Spinal cord contusion causes acute plasma membrane damage. J. Neurotrauma 26 (4), 563–574.
Singleton, R.H., Povlishock, J.T., 2004. Identification and characterization of heterogeneous neuronal injury and death in regions of diffuse brain injury: evidence for multiple independent injury phenotypes. J. Neurosci. 24 (14), 3543–3553.
Slomka, N., Gefen, A., 2012. Relationship between strain levels and permeability of the plasma membrane in statically stretched myoblasts. Ann. Biomed. Eng. 40 (3), 606–618.
Smith, D.H., Lowenstein, D.H., Gennarelli, T.A., Mcintosh, T.K., 1994. Persistent memory dysfunction is associated with bilateral hippocampal damage following experimental brain injury. Neurosci. Lett. 168 (1–2), 151–154.
Smith, D.H., Soares, H.D., Pierce, J.S., Perlman, K.G., Saatman, K.E., Meaney, D.F., Dixon, C.E., McIntosh, T.K., 1995. A model of parasagittal controlled cortical impact in the mouse: cognitive and histopathologic effects. J. Neurotrauma 12 (2), 169–178.
Stone, J.R., Okonkwo, D.O., Dialo, A.O., Rubin, D.G., Mutlu, L.K., Povlishock, J.T., Helm, G.A., 2004. Impaired axonal transport and altered axolemmal permeability occur in distinct populations of damaged axons following traumatic brain injury. Exp. Neurol. 190 (1), 59–69.
Stroetz, R.W., Vlahakis, N.E., Walters, B.J., Schroeder, M.A., Hubmayr, R.D., 2001. Validation of a new live cell strain system: characterization of plasma membrane stress failure. J. Appl. Physiol. 90 (6), 2361–2370.
Tran, L.D., Lifshitz, J., Witgen, B.M., Schwarzbach, E., Cohen, A.S., Grady, M.S., 2006. Response of the contralateral hippocampus to lateral fluid percussion brain injury. J. Neurotrauma 23 (9), 1330–1342.
Vlahakis, N.E., Schroeder, M.A., Pagano, R.E., Hubmayr, R.D., 2002. Role of deformation-induced lipid trafficking in the prevention of plasma membrane stress failure. Am. J. Respir. Crit. Care Med. 166 (9), 1282–1289.
Whalen, M.J., Dalkara, T., You, Z., Qiu, J., Bermpohl, D., Mehta, N., Suter, B., Bhide, P.G., Lo, E.H., Ericsson, M., Moskowitz, M.A., 2008. Acute plasmalemma permeability and protracted clearance of injured cells after controlled cortical impact in mice. J. Cereb. Blood Flow Metab. 28 (3), 490–505.
Yang, K.H., King, A.I., 2003. A limited review of finite element models developed for brain injury biomechanics research. Int. J. Veh. Des. 32, 116–129.
Zhang, L., Yang, K.H., Dwarampudi, R., Omori, K., Li, T., Chang, K., Hardy, W.N., Khalil, T.B., King, A.I., 2001. Recent advances in brain injury research: a new human head model development and validation. Stapp Car Crash J. 45, 369–393.